



Enhanced internal electric field in S-doped BiOBr for intercalation, adsorption and degradation of ciprofloxacin by photoinitiation

Yang Jin ^a, Fan Li ^b, Tong Li ^{b,*}, Xueci Xing ^b, Wenhong Fan ^a, Lili Zhang ^c, Chun Hu ^{a,b}

^a School of Space and Environment, Beihang University, Beijing 100191, China

^b Institute of Environmental Research at Greater Bay, Key Laboratory for Water Quality and Conservation of the Pearl River Delta, Ministry of Education, Guangzhou University, Guangzhou 510006, China

^c Key Laboratory of Drinking Water Science and Technology, Research Center for Eco-Environmental Sciences, Chinese Academy of Sciences, Beijing 100085, China



ARTICLE INFO

Keywords:

S-doped BiOBr
Internal electric field
Intercalation and adsorption
Photo-initiated R[•] radical
CIP degradation

ABSTRACT

A photocatalyst of layered structural BiOBr doped with sulfur (S-BiOBr) was synthesized using a facile hydrothermal method. X-ray powder diffraction, Fourier transform infrared spectroscopy, X-ray photoelectron spectroscopy and density functional theory calculation revealed that S-BiOBr consisted of covalent [Bi₂O₂S]²⁺ layer and exchangeable bromide ions [Br₂]²⁻. The specific layered structure of S-BiOBr exhibited excellent performance for the intercalation, adsorption and photocatalytic degradation of ciprofloxacin (CIP) by forming interlayer [Bi₂O₂S]²⁺-OOC-R complexes. Furthermore, the internal electric field enhanced by polarization effects in the [Bi₂O₂S]²⁺ layer was conducive to a lasting electron transfer in the dark condition after photoactivation. The electron of R[•] radical derived from oxidizing [Bi₂O₂S]-OOC-R persistently migrated to the S-BiOBr surface and was trapped by O₂ to form O₂^{•-}, facilitating the degradation of CIP in the dark. Hence, the degradation of CIP could be realized by utilizing the R[•] radical triggered through transient photoinitiation with low optical energy consumption.

1. Introduction

Semiconductor photocatalysis has received considerable attention because of its eco-friendly nature to address concerns regarding environmental pollution and energy crisis utilizing solar energy [1–3]. During the photocatalytic processes, the photo-generated electron and hole (e-h) pairs are separated by photoexcitation, and subsequently migrate to surface reactive sites across the bulk for pollution degradation. Previous studies have proposed some effective strategies to promote the separation of charge carriers, such as element doping, defect engineering, and heterojunction formation [4–9]. However, with increasing levels of modification, a trapping center is formed for e-h recombination, leading to a limited improvement in photocatalytic efficiency. As a result, the development of photocatalysis is extremely restricted owing to the inefficient utilization of solar energy for the photon-to-electron conversion.

Our previous studies discovered that the interaction between adsorbed pollutants and semiconductor surfaces is beneficial for separating charge carriers to expedite pollutant degradation. For example, the surface complexation of Sb₂S₃ between the azo group and Sb³⁺

enhances the partial charge transfer, thereby causing breakage of the -N=N- bond [10]. In addition, the adsorption of pollutants is strengthened by hydrogen bond and π-π bond interactions on the dual oxygen group (C-O-C and C=O) doped carbon nitride, contributing to improving removal efficiency [11]. Therefore, the construction of a novel interface is important for surface complex adsorption for the photocatalytic degradation of pollutants.

BiOBr is a novel photocatalyst consisting of positive [Bi₂O₂]²⁺ and negative halogen atom (Br₂²⁻) slabs to form a unique layered structure [12–16]. Based on the weak interlayer interaction of van der Waals forces, the layered structures allow variant species (e.g., inorganic anions, organic acids/bases and organic complexes) to intercalate into the interlaminar space by anion exchange. Our findings have revealed that CrO₄²⁻ intercalated in BiOBr with exposed {110} facets provides impurity levels to expand the visible absorption range, promoting direct photoexcitation for the photoreduction of Cr(VI) [17]. Moreover, the internal electric field (IEF) is constructed by a non-uniform polarization charge due to the alternating stacks of the positive and negative layers along the [001] direction [18]. Zhang et al. have reported that IEF tuning by C doping in Bi₃O₄Cl enormously boosts the bulk-charge

* Corresponding author.

E-mail address: litong619@gzhu.edu.cn (T. Li).

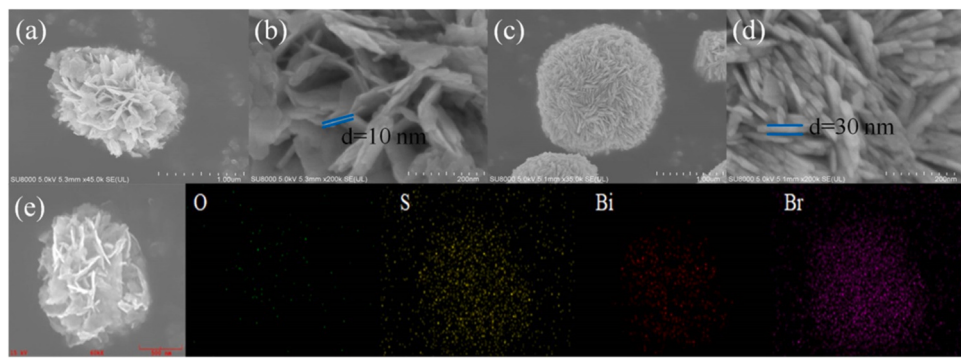


Fig. 1. FESEM images of (a and b) S-BiOBr-3 and (c and d) BiOBr; (e) EDX elemental mapping analysis (O, S, Bi, and Br) of S-BiOBr-3.

transport efficiency [19]. Thus, the approaches of non-metal doping-based IEF tuning are generally favorable for enhancing polarization between layers for oxidizing organic pollutants.

Furthermore, organic pollutants are continuously oxidized to intermediate products, and even to CO_2 by reactive species (h^+ , $\cdot\text{OH}$, and O_2^\bullet) in photocatalytic reactions [20–22]. However, studies on the role of organic radicals (R^\bullet) in photocatalytic processes are still lacking. In traditional photocatalytic reactions, large quantities of organic radicals (R^\bullet) are produced to react with reactive oxygen species (ROS) [23,24]. However, recently, Lyv et al. have found that in a Fenton-like reaction of d-TiCuAl-SiO₂Ns with dual reaction centers, the organic radicals (R^\bullet) donate electrons to the electron-deficient center (anode), followed by electron transfer to the electron-rich center (cathode) to improve H_2O_2 utilization efficiency [25]. These results suggest that R^\bullet could probably be oxidized through the interaction between R^\bullet and the interface of photocatalysts instead of ROS.

Herein, BiOBr modified with different amounts of S (S-BiOBr) was synthesized through a facile hydrothermal method to regulate the IEF, inducing polarization effects between layers. The degradation of ciprofloxacin (CIP) was investigated by switching the light on and off to explore the role of R^\bullet radicals. Interestingly, CIP could be continuously degraded in the dark because of the interaction between R^\bullet and the interface of photocatalysts after the initial light irradiation. Hence, this study derived a radically new approach, in which CIP was degraded by utilizing the R^\bullet radical with transient illumination to reduce optical energy consumption.

2. Experimental section

2.1. Materials

All chemical reagents used in this study were of analytical grade. Bismuth nitrate pentahydrate ($\text{Bi}(\text{NO}_3)_3 \cdot 5\text{H}_2\text{O}$), potassium bromide (KBr), glycol, ethanol, Ciprofloxacin (CIP), BMPO and dimethyl sulfoxide were purchased from Sinopharm Chemical Reagent Co., Ltd.

2.2. Preparation of S-doped BiOBr

Typically, S-doped BiOBr was synthesized as follows: $\text{Bi}(\text{NO}_3)_3 \cdot 5\text{H}_2\text{O}$ (3 mmol) and KBr (3 mmol) were dissolved in 30 mL of ethylene glycol to homogenize for 30 min at room temperature. Thiourea (0, 50, 100, 150, and 200 mg) as sulfur source was separately added to the BiOBr precursor solution under vigorous stirring, generating S-BiOBr-x (x = 0, 1, 2, 3, and 4). The mixed solution was transferred into a 50 mL teflon-lined stainless steel autoclave and heated at 160 °C for 12 h. The products were collected, washed thrice with water and ethyl alcohol, and subsequently dried under vacuum for 6 h at 60 °C.

2.3. Characterization

The crystal phases of BiOBr with different S contents were investigated by X-ray powder diffraction (XRD) using a diffractometer (Scintag-XDS-2000) with $\text{Cu K}\alpha$ radiation. Fourier transform infrared spectroscopy (FTIR) of S-BiOBr was performed by a Bruker Tensor 27 spectrophotometer. The morphology of the samples was observed using an SU-8020 field emission scanning electron microscope (FESEM, Hitachi). The surface elements of the samples were analyzed by X-ray photoelectron spectroscopy (XPS) using the Krato AXIS Ultra instrument (Kratos) with monochromatic Al $\text{K}\alpha$ radiation (225 W, 15 mA, 15 kV). Photoluminescence spectra were obtained on an Edinburgh FLS-980 fluorescence spectrometer. The electron spin resonance signals of the spin-trapped oxidative radicals were measured on an ESP 300 electron paramagnetic resonance spectrometer (Bruker) with BMPO spin-trap reagent. Photoelectrochemical measurements of the samples were performed by a CHI 660D electrochemical workstation with a conventional three-electrode cell system, which was connected to a photocatalyst working electrode and Pt counter electrode in 0.1 M Na_2SO_4 solution.

2.4. Theoretical computation section

First principle calculations were performed by density functional theory using the Vienna ab initio simulation package [26]. The generalized gradient approximation with the Perdew Burke Ernzerh exchange-correlation functional was used to describe the electronic exchange and correlation effects. Uniform G-centered k-point meshes with a resolution of $2\pi \times 0.03 \text{ \AA}^{-1}$ and Methfessel-Paxton electronic smearing were adopted for integration in the Brillouin zone for geometric optimization [27,28]. The simulation was run with cut-off energy of 500 eV throughout the computations. These settings ensure convergence of the total energies to within 1 meV per atom. Structural relaxation proceeded until all forces on atoms were less than 1 meV \AA^{-1} and the total stress tensor was within 0.01 GPa of the target value.

2.5. Evaluation of photocatalytic performance

The photocatalytic activity of the samples was determined by the degradation of CIP under an LED lamp (PCX50C Discover reaction system, Beijing Perfectlight Technology Co., Ltd. $\lambda > 420 \text{ nm}$, light intensity = 100 mW cm^{-2}). Typically, 50 mg of the sample was added to 50 mL of 10 mg L^{-1} CIP solution under vigorous stirring in the dark for 30 min to establish the adsorption-desorption equilibrium. The suspension was then exposed to visible light for the photocatalytic oxidation of CIP. At specific time intervals, 1 mL of the solution sample was collected and filtered through a 0.45 μm membrane. The concentration of CIP in solution was measured by high-performance liquid chromatography (1200 series; Agilent Technologies) with a ZORBA SB-Aq column (5 μm , 4.6 × 250 mm; Agilent Technologies).

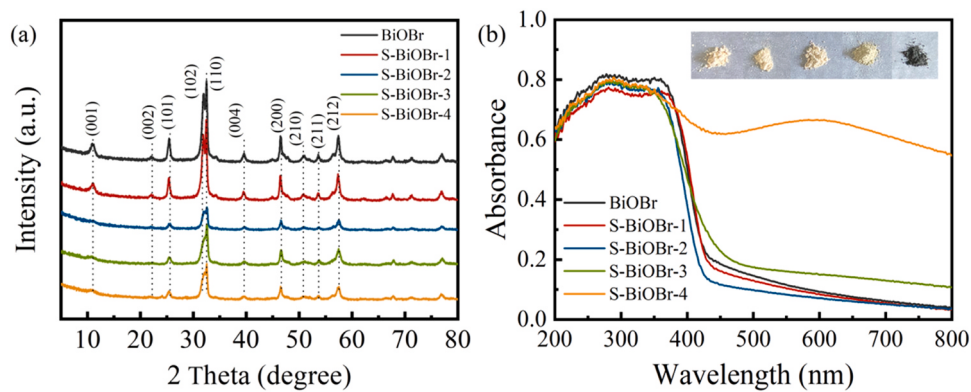


Fig. 2. (a) XRD patterns and (b) UV-visible diffuse reflectance spectra of S-BiOBr-x ($x = 0, 1, 2, 3$, and 4).

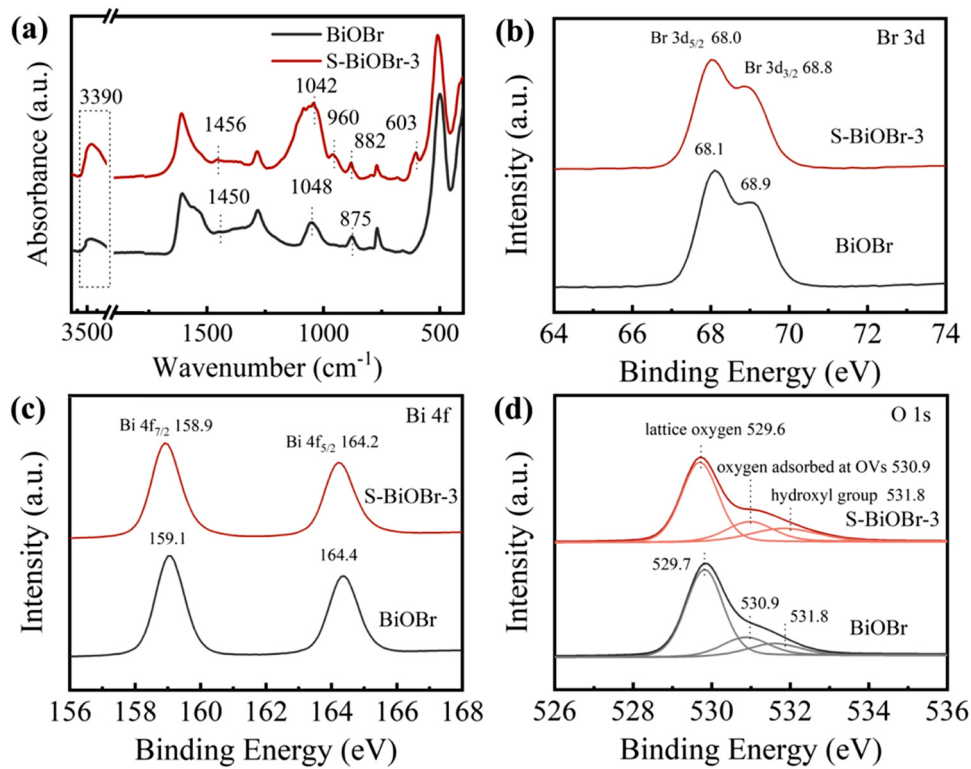


Fig. 3. (a) FTIR spectra and (b) Br 3d, (c) Bi 4f, and (d) O 1s XPS spectra of BiOBr and S-BiOBr-3.

3. Results and discussion

3.1. Morphology and structure

FESEM images (Fig. 1a and b) showed that the S-BiOBr-3 sample had a loose flower-like structure composed of nanosheets with a thickness of approximately 10 nm. In contrast to BiOBr (approximately 30 nm) (Fig. 1c and d), the thinner nanosheets resulted from the strong interaction of doped S atoms with Bi, which affected the stacking of $[Bi_2O_2]^{2+}$ and $[Br_2]^{2-}$ slabs by inhibiting the growth of crystal nucleus. The introduction of S resulted in a larger interlayer distance, contributing to the ultrathin nanosheets. In addition, mapping of S-BiOBr-3 using energy dispersive spectroscopy showed the uniform distribution of Bi, O, Br, and S atom, indicating even doping of S atoms in the BiOBr structure (Fig. 1e).

XRD patterns of S-BiOBr-x ($x = 0, 1, 2, 3$, and 4) are shown in Fig. 2a. The diffraction peaks at 10.8° , 25.4° , 31.9° , 32.4° , 46.4° and 57.3° were assigned to the (001), (101), (102), (110), (004), and (212) crystal,

respectively, which was consistent with the standard diffraction patterns of tetragonal BiOBr (JCPDS Card No. 73-2061) [29]. However, with an escalating amount of S doping, the intensity of all peaks was significantly weakened without detection of any impurity, indicating the high stability and reliability of the S-doped BiOBr structure, causing no phase transition of the BiOBr nanocrystals. Moreover, the characteristic peak of the (001) facet gradually moved in a low-angle direction, implying the expansion of the interlayer space owing to S doping [30]. The effective amount of S doping in BiOBr was accurately determined by X-ray fluorescence spectroscopy, and the mass ratio of S to S-BiOBr-x ($x = 0, 1, 2, 3$, and 4) was 0.17%, 0.28%, 0.97%, and 2.74%, respectively (Table S1).

The optical absorption properties of S-BiOBr-x ($x = 0, 1, 2, 3$, and 4) were comprehensively investigated by UV-visible diffuse reflectance spectroscopy to reveal the role of S doping (Fig. 2b). The optical absorption of S-BiOBr-1 and S-BiOBr-2 was almost the same as that of pristine BiOBr (~ 420 nm), while that of S-BiOBr-3 exhibited a broader optical absorption range, extending from 420 to 480 nm. The

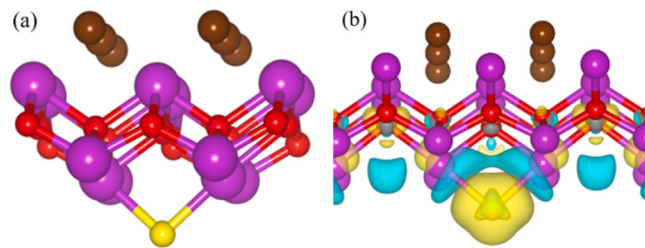


Fig. 4. (a) The geometric structure and (b) charge distribution of S-BiOBr-3.

corresponding band gap calculated by the plots of $(ahv)^{1/2}$ versus $h\nu$, was dramatically reduced from 2.64 to 2.16 eV (Fig. S1), suggesting that homogeneous S doping in the bulk structure enabled BiOBr with a narrow intrinsic band gap due to the stronger binding affinity of S^{2-} ions and heavy metal Bi^{3+} . However, with the increase in S doping, accompanied by a color change from white to black, S-BiOBr-4 exhibited a narrower band gap than other S-BiOBr-x, which would probably induce the extensive recombination of photo-induced e-h pairs, resulting in serious negative effects on photocatalytic performance.

The FTIR spectrum of S-BiOBr-3 displayed two new peaks at 603 and 960 cm^{-1} which were identified as Bi—S bond vibrations (Fig. 3a) [31, 32]. This finding confirms that the doped S atom was strongly bound to Bi. In addition, the asymmetric and symmetric stretching vibration peaks of the Bi-Br band at 1450 and 1048 cm^{-1} shifted to 1456 and 1042 cm^{-1} , respectively [33,34], implying that the interlayer $[Br^-]$ might be occupied by S atoms. The slight red-shift peak of Bi-O bending vibration at 882 cm^{-1} suggested that the Bi—S bond had a significant impact on the combination of $[Bi_2O_2]^{2+}$ slabs, as noted previously [35]. In addition, peaks at 3390 and 1605 cm^{-1} originating from the stretching and flexural vibrations of -OH, respectively [36], were noted to be remarkably strengthened in this study based on the large interlayer space in the S-BiOBr-3 structure.

The XPS spectra of S-BiOBr-3 were applied to analyze the functional effects of S-doped structures. The Br 3d peaks repositioned from 68.1

and 68.9 eV to 68.0 and 68.8 eV, respectively, indicating that the Br^- was replaced with S^{2-} by anion exchange due to weakened van der Waals force between $[Br_2]^{2-}$ slabs (Fig. 3b) [37]. The corresponding Bi 4f peaks (Fig. 3c) appearing at 158.9 and 164.2 eV for Bi 4f_{7/2} and Bi 4f_{5/2}, respectively, displaced by 0.2 eV towards lower binding energy, suggesting a noticeable electronic offset from S to Bi via Bi—S bond. Moreover, the O1s peaks (Fig. 3d) at 529.6, 530.9, and 531.8 eV are typified for lattice oxygen, adsorbed oxygen species at the vacant sites, and surface hydroxyl groups, respectively [38]. Compared with that in BiOBr, the peak of lattice oxygen decreased by 0.1 eV, along with a significant increase in the ratio of oxygen adsorbed to lattice oxygen at the vacancies (OVs) from 25.2% to 35.4%, indicating more adsorption of O_2 molecule on the oxygen-vacant sites after S doping. These results confirmed that the S doped in the interlayer established a connection with Bi in $[Bi_2O_2]^{2+}$ to form $[Bi_2O_2S]^{2+}$ layers, inducing even more structural defects at the O site in the $[Bi_2O_2]$ layer to produce abundant OVs. Moreover, the structural rearrangement of $[Bi_2O_2S]^{2+}$ and $[Br_2]^{2-}$ slabs was conducive to enhancing the polarization effects between the layers for rapid charge transfer. The geometric structural model of S-doped BiOBr with interlaced $[Bi_2O_2S]^{2+}$ and $[Br_2]^{2-}$ layers is shown in Fig. 4a. First principles calculations based on density functional theory were performed to illustrate the polarization of the non-uniform charge distribution between the layers (Fig. 4b). The less electronegative S atom substituted the Br atom, forming a high charge density in the $[Bi_2O_2S]^{2+}$ slabs. The strong Bi—S bond contributed to electron accumulation and depletion on S and Bi atoms, respectively, leading to powerful polarization between layers. To some extent, polarization could improve the intrinsic IEF as a driving force for the separation and transport of charge carriers.

Furthermore, the OVs on the catalyst can be characterized by electron paramagnetic resonance for the detection of unpaired electrons. As depicted in Fig. 5a, a relatively strong signal peak at 2.004 was recorded in S-BiOBr-3, corresponding to the abundance of unpaired electrons, suggesting the presence of massive OV defects in $[Bi_2O_2S]^{2+}$, which has been ascribed to the incorporation of S into $[Bi_2O_2]^{2+}$ slabs [39]. In

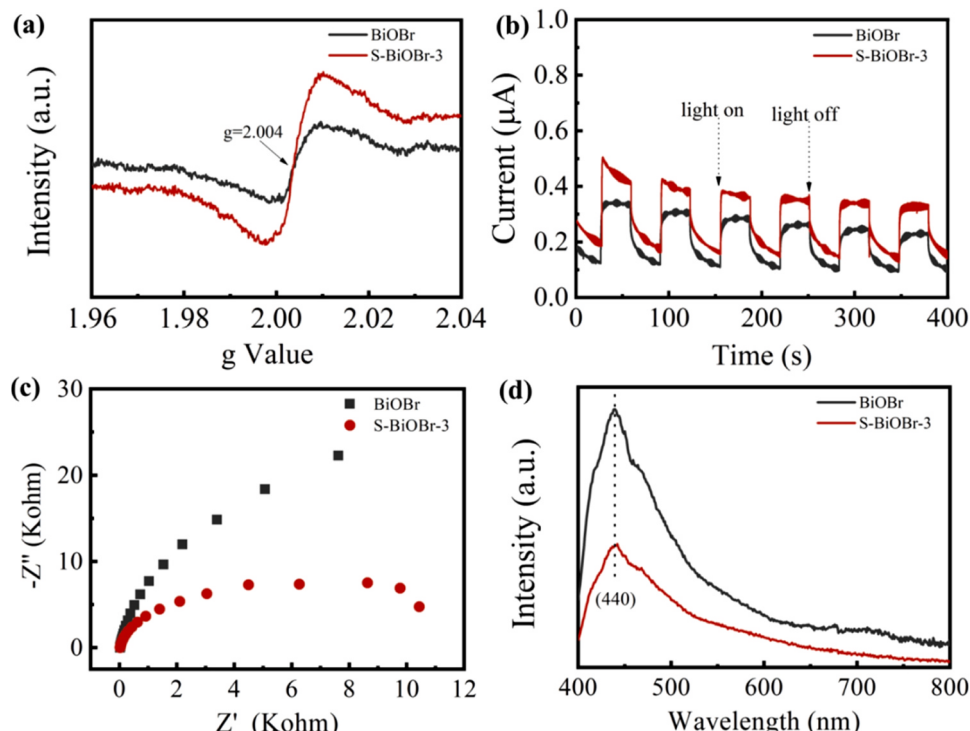


Fig. 5. (a) Electron spin resonance spectra (EPR); (b) transient photocurrent responses; (c) electrochemical impedance spectroscopy Nyquist plots and (d) photoluminescence spectra of BiOBr and S-BiOBr-3.

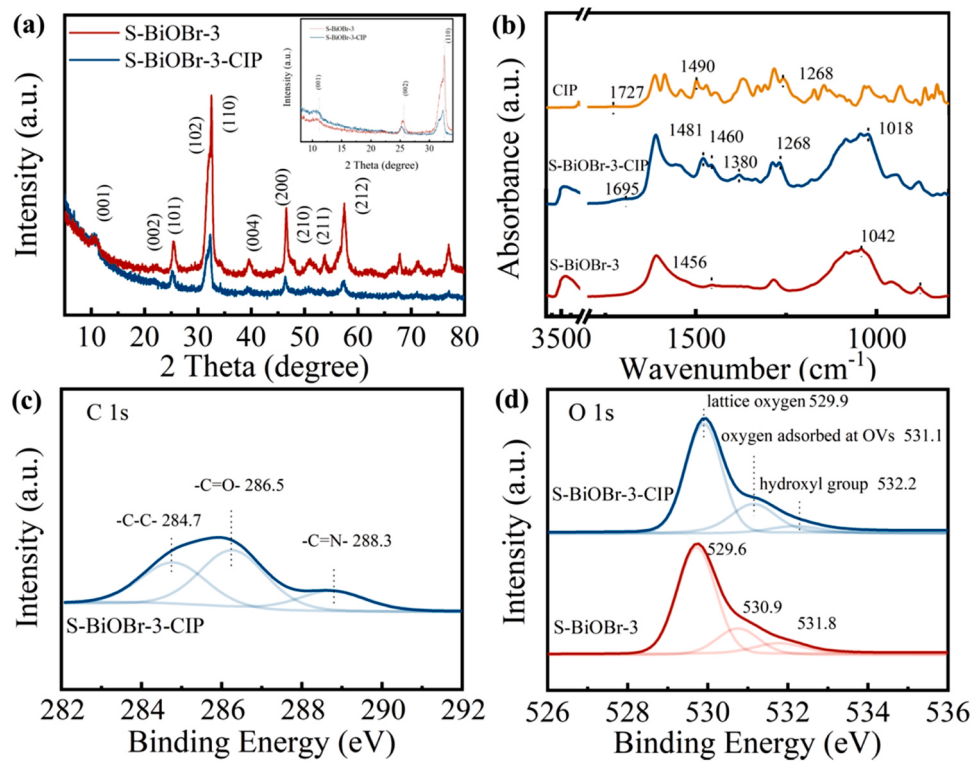


Fig. 6. (a) XRD patterns, (b) FTIR spectra, (c) C 1s XPS spectra and (d) O 1s XPS spectra of S-BiOBr-3 before and after CIP adsorption.

addition, the photo-ionized oxygen vacancies (OVs^+) could persistently capture electrons, as trap sites, and rapidly transport them under the effects of polarization between the $[\text{Bi}_2\text{O}_2\text{S}]^{2+}$ and $[\text{Br}_2]^{2-}$ layers. Electrochemical measurements showed that the photocurrent intensity of S-BiOBr-3 was nearly 1.5 times higher than that of BiOBr, demonstrating that the $[\text{Bi}_2\text{O}_2\text{S}]^{2+}$ structure formed by lattice doping of S favored the separation of photo-generated e-h pairs (Fig. 5b). The electrochemical impedance spectroscopy analysis exhibited a smaller Nyquist circle in S-BiOBr-3 than in BiOBr (Fig. 5c), implying a higher efficiency for interfacial charge transfer. The photoluminescence spectra of S-BiOBr-3 (Fig. 5d) illustrated that the intensity of the characteristic band at 440 nm was evidently weakened. This finding confirmed the function of the S-doped structure, which was to reduce the e-h pair recombination inside S-BiOBr-3. Therefore, the polarization between the layers and OV defects caused by the $[\text{Bi}_2\text{O}_2\text{S}]^{2+}$ slabs were indeed beneficial for charge separation and charge transfer.

3.2. Interaction between CIP and S-BiOBr-3

The adsorption mechanism of CIP on S-BiOBr-3 surfaces was investigated to understand the interaction between them. Approximately

64.3% of the CIP adsorbed on S-BiOBr-3 within 30 min, which was considerably higher than that on BiOBr (35.1%), indicating that the more open architecture facilitated by S doping provided more adsorption sites for CIP (Fig. S2). Moreover, the CIP adsorption rate was rapid for the first 5 min and gradually reached equilibrium in less than 10 min, possibly because of the great affinity between CIP and S-BiOBr-3. The XRD pattern of S-BiOBr-3 with CIP adsorption showed that the diffraction peak positions of (001), (002) and (110) shifted from 10.7° , 25.5° , and 32.4° to 10.4° , 25.2° , and 32.2° , respectively (Fig. 6a). Such a shift reflected the interlayer structural changes attributed to the intercalated adsorption of CIP between layers owing to the expansion of the interlayer space in S-BiOBr-3. Fig. 6b show the FTIR spectrum of CIP-adsorbed S-BiOBr-3, in which two extra peaks at 1268 and 1481 cm^{-1} , corresponding to the aromatic ring bond belonging to CIP, were detected. The -OH peak at 3390 cm^{-1} moved to 3490 cm^{-1} with a weak intensity, and both the peaks for Bi-Br at 1456 and 1042 cm^{-1} shifted to 1460 and 1018 cm^{-1} , respectively. The changes in the vibration bands of the interlayer anions, including Br^- and OH^- , illustrated that the adsorbed CIP was predominantly intercalated in anionic areas between layers due to the negatively charged carboxyl (-COO) group of CIP. Moreover, the peak at 1727 cm^{-1} , which represents the -COOH group of

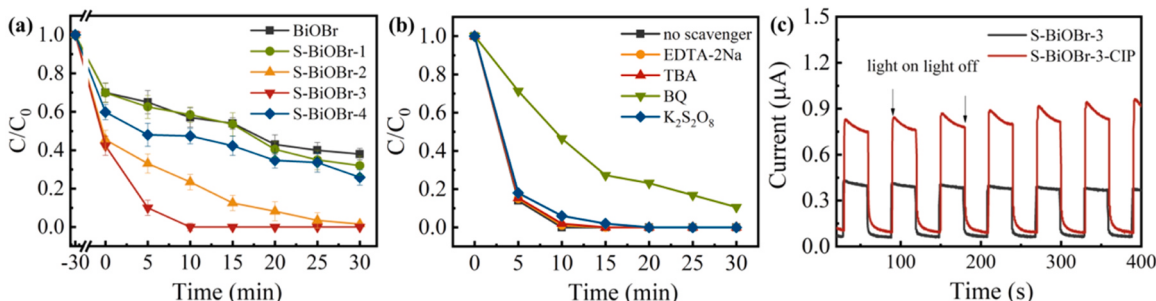


Fig. 7. (a) Photodegradation of CIP in S-BiOBr-x ($x = 0, 1, 2, 3$, and 4) suspensions under visible light irradiation (CIP: 10 ppm; photocatalyst: 1.0 g/L); (b) active species trapping experiments with S-BiOBr-3; (c) transient photocurrent response of S-BiOBr-3 before and after CIP adsorption.

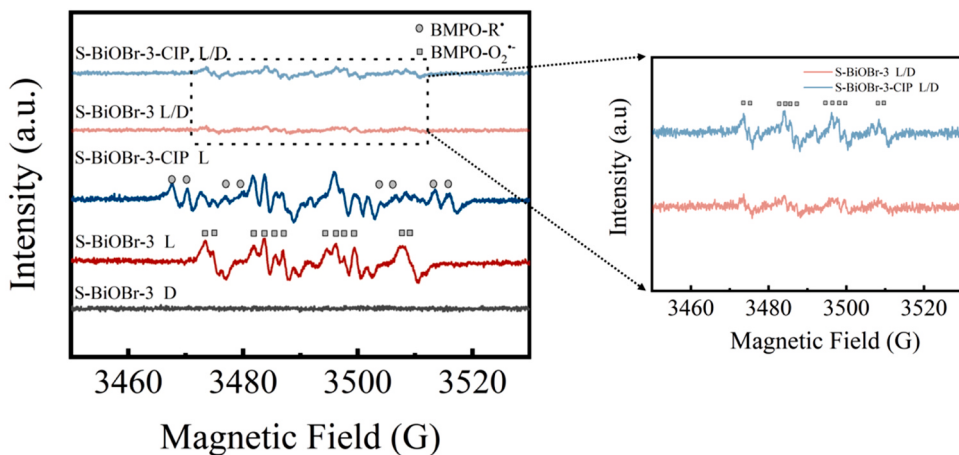


Fig. 8. Electron paramagnetic resonance spectra for BMPO spin trapping of O_2^{\bullet} and R^{\bullet} in S-BiOBr-3 with/without CIP adsorption. (L: light; D: darkness; L/D: the system was first exposed to visible light irradiation, followed by darkness).

CIP, was split into two bands at 1695 and 1380 cm^{-1} . These results indicated the presence of $[\text{Bi}_2\text{O}_2\text{S}]^{2+}\text{-CIP}$ complex involving monodentate linkages via -COO⁻ group of CIP with the $[\text{Bi}_2\text{O}_2\text{S}]^{2+}$ layers [40].

The C 1s spectra of S-BiOBr-3-CIP with a high intensity at 284.7, 286.5 and 288.3 eV were identified as the -C-C-, -C-O- and -C=N- bands of CIP, respectively (Fig. 6c). Moreover, the O 1s characteristic peak for CIP-adsorbed S-BiOBr-3 shifted from 529.6, 530.9, and 531.8 eV to 529.9, 531.1, and 532.2 eV, respectively (Fig. 6d), while the ratio of the hydroxyl group to lattice oxygen decreased from 10.5% to 6.3%, indicating replacement of hydroxyl groups between layers with -COOH group of CIP. As a result, the -COO⁻ group of CIP was preferentially intercalated into S-BiOBr-3 by exchange with OH⁻, leading to the formation of $[\text{Bi}_2\text{O}_2\text{S}]^{2+}\text{-OOC-R}$ (S-BiOBr-3-CIP) complex between the layers.

3.3. Mechanism of CIP degradation

The photocatalytic degradation of CIP on S-BiOBr-x was executed under an LED lamp ($\lambda = 420\text{--}780\text{ nm}$) with a light intensity of 100 mW cm^{-2} (Fig. 7a). CIP was almost completely removed in the S-BiOBr-3 suspensions, whereas only 34.9% of the CIP was degraded in BiOBr suspension within 10 min. Degradation curves for all samples followed pseudo-first-order kinetics, with a kinetic rate constant (k) of 0.2303 min^{-1} in S-BiOBr-3 suspension, which was almost 10.45, 8.32, 2.09 and 9.19 times higher than that in BiOBr, S-BiOBr-1, S-BiOBr-2, and S-BiOBr-4, respectively (Fig. S3). The excellent photocatalytic performance of S-doped BiOBr for CIP degradation was ascribed to the construction of $[\text{Bi}_2\text{O}_2\text{S}]^{2+}$ layers, which possessed prominent IEF properties for charge separation and charge transfer. Repeated tests with several cycles of photocatalytic CIP degradation by S-BiOBr-3 were conducted. The removal of CIP by S-BiOBr-3 remained over 90% within 20 min even after five cycles, exhibiting outstanding photocatalytic activity, although it was slightly less than the initial value obtained (Fig. S4). The corresponding characterization of S-BiOBr-3 after cyclic tests was better described by FESEM, XRD, FTIR, and XPS analysis. There was no change in morphology and structure of S-BiOBr-3, indicating predominant stability.

To identify the reactive species responsible for photocatalytic CIP oxidation in S-BiOBr-3, radical trapping experiment was conducted as shown in Fig. 7b. ethylenediamine tetraacetic acid disodium salt (EDTA-2Na), $\text{K}_2\text{S}_2\text{O}_8$, tert-butyl alcohol (TBA) and p-benzoquinone (BQ) were used as scavengers for photo-excited holes (h^+), photo-excited electron (e^-), $\cdot\text{OH}$, and O_2^{\bullet} , respectively. The degradation of CIP was significantly inhibited by the introduction of BQ, suggesting that O_2^{\bullet} was the main reactive oxygen species involved in the photocatalytic oxidation of

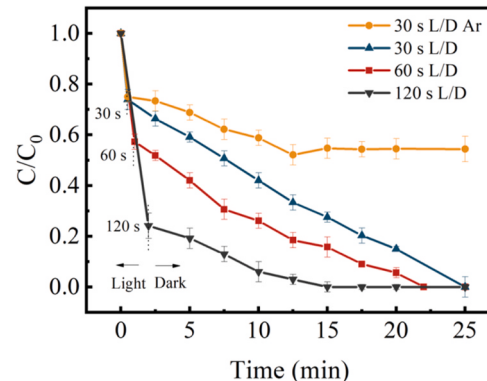


Fig. 9. Removal efficiency of CIP by S-BiOBr-3 in the dark after 30, 60, and 120 s of illumination.

CIP. However, the presence of other scavengers barely resulted in difference in CIP removal, indicating no involvement of the interfacial transfer of electrons and holes during CIP degradation. Fig. 7c shows a significant increase in the photocurrent response of S-BiOBr-3 in the presence of CIP. As CIP was predominantly intercalated between the layers of S-BiOBr-3 to form the $[\text{Bi}_2\text{O}_2\text{S}]^{2+}\text{-OOC-R}$ complex, it is accessible to the photo-excited holes (h^+) in the bulk. Upon direct oxidation of h^+ , the $[\text{Bi}_2\text{O}_2\text{S}]^{2+}\text{-OOC-R}$ complex could be readily transformed into $[\text{Bi}_2\text{O}_2\text{S}]^{2+}\text{-OOC-R}^{\bullet}$, involving a potential decarboxylation process. Accordingly, massive quantities of electrons migrated to the surface along with the oxidization of CIP under exposure to visible light. Furthermore, an increase in dark current was observed in S-BiOBr-3 with intercalated CIP, indicating that the electrons derived from $[\text{Bi}_2\text{O}_2\text{S}]^{2+}\text{-OOC-R}^{\bullet}$ could be continuously transported to the S-BiOBr-3 surface after switching off the light.

The spin-trapping technique was adopted to probe reactive radical species with BMPO in DMSO solution using EPR (Fig. 8). The signal of BMPO- O_2^{\bullet} with twelve characteristic peaks appeared on S-BiOBr-3 surface in the absence of CIP under visible light [41]. In addition to the high intensity of BMPO- O_2^{\bullet} , eight additional characteristic peaks were observed for CIP-adsorbed S-BiOBr-3, possibly attributed to the R^{\bullet} radical. On the contrary, after switching off the light, BMPO was added to capture reactive species in the dark. The signal of BMPO- O_2^{\bullet} in the S-BiOBr-3 suspensions with CIP was significantly enhanced, whereas the eight characteristic peaks almost disappeared. Based on these results, we concluded that the electrons of R^{\bullet} radical from the interlayer $[\text{Bi}_2\text{O}_2\text{S}]^{2+}\text{-OOC-R}^{\bullet}$ complex were transferred to the S-BiOBr-3 surface driven

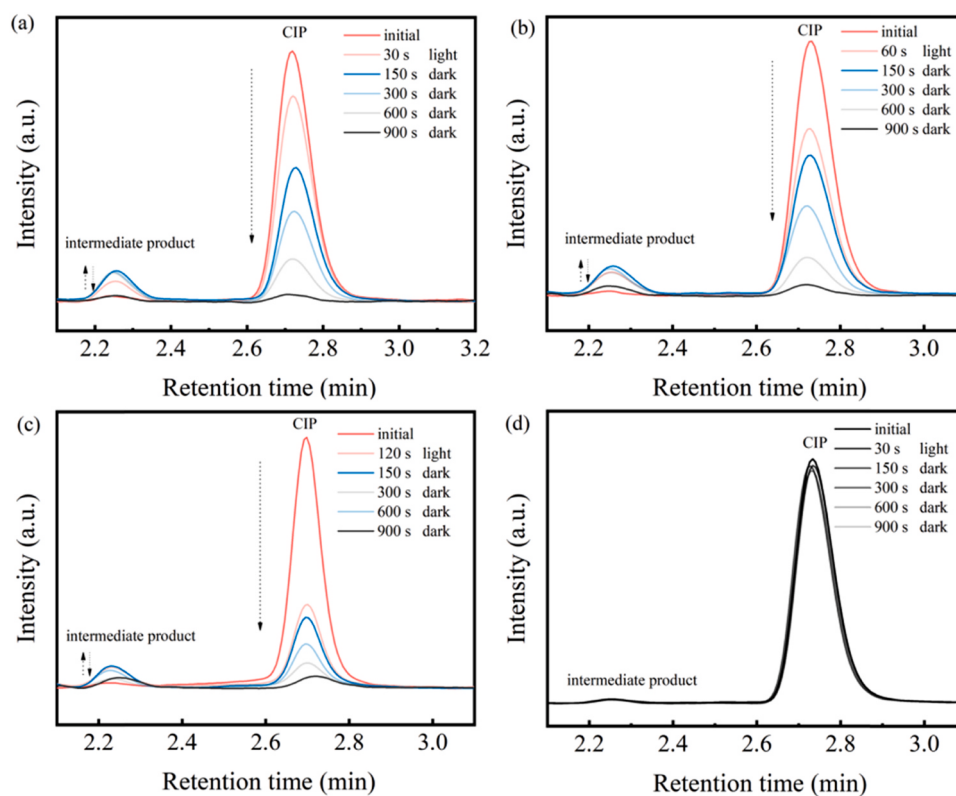


Fig. 10. (a) High-performance liquid chromatography (HPLC) analysis of CIP degradation by S-BiOBr-3 after (a) 30, (b) 60, and (c) 120 s visible light irradiation; (d) HPLC analysis of CIP degradation in BiOBr suspension after 30 s visible light irradiation.

by the polarized IEF of $[Bi_2O_2S]^{2+}$ layers, facilitating the formation of $O_2^{\bullet-}$ radicals in the dark.

The degradation of CIP by S-BiOBr-3 in the dark was further detected after 30, 60, and 120 s illumination (Fig. 9). Interestingly, CIP could be continuously oxidized under all dark reaction and ultimately, completely removed within 25 min. The consumption of optical energy in this case was significantly less than that under continuous illumination. The peak for intermediate products (CIP^*) was observed by high-performance liquid chromatography, which showed an initial accumulation that was followed by a drop in the peak height (Fig. 10). The transformation of CIP into intermediate product (CIP^*) reflected the R^{\bullet} radical formation, which was consistent with EPR results. Additionally, the oxidation of CIP was suppressed in an inert argon atmosphere, indicating that O_2 was critical for CIP degradation under dark conditions. These results confirmed that under the polarized IEF of $[Bi_2O_2S]^{2+}$ layers, substantial amounts of electrons arising from the R^{\bullet} radical could sequentially migrate to the S-BiOBr-3 surface, where O_2 was reduced to $O_2^{\bullet-}$, a major contributor to CIP oxidation under dark conditions. Therefore, CIP degradation independent of continuous illumination with low optical energy consumption was attributed to the $O_2^{\bullet-}$ formed by interaction of the R^{\bullet} and the IEF. In contrast, a similar phenomenon was not observed for BiOBr (Fig. S5), suggesting that the traditional photocatalytic degradation of CIP relied heavily on the external optical energy input.

4. Conclusions

In conclusion, a layered S-doped BiOBr photocatalyst was devised to enhance the polarization between the $[Bi_2O_2S]^{2+}$ and $[Br_2]^{2-}$ layers to improve IEF, expediting the separation of photo-generated charge carriers. Moreover, the open-channel structure of S-doped BiOBr was conducive to the CIP ($OOC-R$) adsorption by intercalation of the carboxyl group (chemical coordination of $[Bi_2O_2S]-OOC-R$). Depending

on the interlayer polarization effects, high-efficiency electron transfer promoted the formation of h^+ in the bulk and $O_2^{\bullet-}$ for CIP oxidation. Furthermore, the residual electrons of the R^{\bullet} radical originating from the oxidized $[Bi_2O_2S]-OOC-R$ complex could be directly migrated to the S-BiOBr-3 surface and trapped by O_2 to generate $O_2^{\bullet-}$ in dark conditions, promoting the degradation of CIP. The cyclic procedures of electron transfer from the R^{\bullet} radical to $O_2^{\bullet-}$ enable complete removal of the CIP with low optical energy consumption by virtue of photoinitiation. Therefore, photocatalysis using S-BiOBr exhibits great potential for applications in wastewater treatment, where photo-activated R^{\bullet} radicals are utilized to remove organic pollutants with much less optical energy input.

CRediT authorship contribution statement

Yang Jin: Methodology, Data curation, Formal analysis, Writing – original draft. **Fan Li:** Supervision, Investigation, Writing – review & editing. **Tong Li:** Conceptualization, Resources, Formal analysis, Funding acquisition, Writing – review & editing. **Xueci Xing:** Resources, Writing – review & editing. **Wenhong Fan:** Resources. **Lili Zhang:** Resources. **Chun Hu:** Funding acquisition, Project administration, Formal analysis, Writing – review & editing.

Declaration of Competing Interest

The authors declare that they have no known competing financial interests or personal relationships that could have appeared to influence the work reported in this paper.

Acknowledgments

This work was funded by China Postdoctoral Science Foundation (Grant Nos. 2019M652841 and 2020T130128), and the National

Natural Science Foundation of China (Grant Nos. 21906034, 51838005 and 51538013).

Appendix A. Supporting information

Supplementary data associated with this article can be found in the online version at doi:10.1016/j.apcatb.2021.120824.

References

- [1] K. Zhao, L. Zhang, J. Wang, Q. Li, W. He, J.J. Yin, Surface structure-dependent molecular oxygen activation of BiOCl single-crystalline nanosheets, *J. Am. Chem. Soc.* 135 (2013) 15750–15753.
- [2] M. Guan, C. Xiao, J. Zhang, S. Fan, R. An, Q. Cheng, J. Xie, M. Zhou, B. Ye, Y. Xie, Vacancy associates promoting solar-driven photocatalytic activity of ultrathin bismuth oxychloride nanosheets, *J. Am. Chem. Soc.* 135 (2013) 10411–10417.
- [3] M. Pan, H. Zhang, G. Gao, L. Liu, W. Chen, Facet-dependent catalytic activity of nanosheet-assembled bismuth oxyiodide microspheres in degradation of bisphenol A, *Environ. Sci. Technol.* 49 (2015) 6240–6248.
- [4] Q. Wang, Z. Liu, D. Liu, G. Liu, M. Yang, F. Cui, W. Wang, Ultrathin two-dimensional BiOBr_xI_{1-x} solid solution with rich oxygen vacancies for enhanced visible-light-driven photoactivity in environmental remediation, *Appl. Catal. B: Environ.* 236 (2018) 222–232.
- [5] L. Ye, J. Liu, Z. Jiang, T. Peng, L. Zan, Facets coupling of BiOBr-g-C₃N₄ composite photocatalyst for enhanced visible-light-driven photocatalytic activity, *Appl. Catal. B: Environ.* 142–143 (2013) 1–7.
- [6] Y. Liang, S. Lin, L. Liu, J. Hu, W. Cui, Oil-in-water self-assembled Ag@AgCl QDs sensitized Bi₂WO₆: enhanced photocatalytic degradation under visible light irradiation, *Appl. Catal. B: Environ.* 164 (2015) 192–203.
- [7] Q. Yan, X. Xie, Y. Liu, S. Wang, M. Zhang, Y. Chen, Y. Si, Constructing a new Z-scheme multi-heterojunction photocatalysts Ag-AgI/BiOI-Bi₂O₃ with enhanced photocatalytic activity, *J. Hazard. Mater.* 371 (2019) 304–315.
- [8] Y. Feng, L. Li, J. Li, J. Wang, L. Liu, Synthesis of mesoporous BiOBr 3D microspheres and their photodecomposition for toluene, *J. Hazard. Mater.* 192 (2011) 538–544.
- [9] J. Cao, W. Nie, L. Huang, Y. Ding, K. Lv, H. Tang, Photocatalytic activation of sulfite by nitrogen vacancy modified graphitic carbon nitride for efficient degradation of carbamazepine, *Appl. Catal. B: Environ.* 241 (2019) 18–27.
- [10] F. Li, L. Zhang, C. Hu, X. Xing, B. Yan, Y. Gao, L. Zhou, Enhanced azo dye decolorization through charge transmission by σ-Sb³⁺-azo complexes on amorphous Sb₂S₃ under visible light irradiation, *Appl. Catal. B: Environ.* 240 (2019) 132–140.
- [11] F. Li, M. Han, Y. Jin, L. Zhang, T. Li, Y. Gao, C. Hu, Internal electric field construction on dual oxygen group-doped carbon nitride for enhanced photodegradation of pollutants under visible light irradiation, *Appl. Catal. B: Environ.* 256 (2019), 117705.
- [12] H. Li, J. Shang, Z. Ai, L. Zhang, Efficient visible light nitrogen fixation with biobr nanosheets of oxygen vacancies on the exposed {001} facets, *J. Am. Chem. Soc.* 137 (2015) 6393–6399.
- [13] M. Shi, G. Li, J. Li, X. Jin, X. Tao, B. Zeng, E.A. Pidko, R. Li, C. Li, Intrinsic facet-dependent reactivity of well-defined BiOBr nanosheets on photocatalytic water splitting, *Angew. Chem. Int. Ed. Engl.* 59 (2020) 6590–6595.
- [14] Y. Wang, Y. Long, Z. Yang, D. Zhang, A novel ion-exchange strategy for the fabrication of high strong BiOI/BiOBr heterostructure film coated metal wire mesh with tunable visible-light-driven photocatalytic reactivity, *J. Hazard. Mater.* 351 (2018) 11–19.
- [15] S. Huang, G. Wang, J. Liu, C. Du, Y. Su, A novel CuBi₂O₄/BiOBr direct Z-scheme photocatalyst for efficient antibiotics removal: synergy of adsorption and photocatalysis on degradation kinetics and mechanism insight, *ChemCatChem* 12 (2020) 4431–4445.
- [16] R. Hou, Y. Gao, H. Zhu, G. Yang, W. Liu, Y. Huo, Z. Xie, H. Li, Coupling system of Ag/BiOBr photocatalysis and direct contact membrane distillation for complete purification of N-containing dye wastewater, *Chem. Eng. J.* 317 (2017) 386–393.
- [17] T. Li, Y. Gao, L. Zhang, X. Xing, X. Huang, F. Li, Y. Jin, C. Hu, Enhanced Cr(VI) reduction by direct transfer of photo-generated electrons to Cr 3d orbitals in CrO₄²⁻-intercalated BiOBr with exposed (110) facets, *Appl. Catal. B: Environ.* 277 (2020), 119065.
- [18] J. Li, L. Cai, J. Shang, Y. Yu, L. Zhang, Giant enhancement of internal electric field boosting bulk charge separation for photocatalysis, *Adv. Mater.* 28 (2016) 4059–4064.
- [19] J. Li, L. Zhang, Y. Li, Y. Yu, Synthesis and internal electric field dependent photoreactivity of Bi₃O₄Cl single-crystalline nanosheets with high {001} facet exposure percentages, *Nanoscale* 6 (2014) 167–171.
- [20] D. Mao, J. Yuan, X. Qu, C. Sun, S. Yang, H. He, Size tunable Bi₃O₄Br hierarchical hollow spheres assembled with {0 0 1}-facets exposed nanosheets for robust photocatalysis against phenolic pollutants, *J. Catal.* 369 (2019) 209–221.
- [21] J.-y Zhu, Y.-p Li, X.-j Wang, J. Zhao, Y.-s Wu, F.-t Li, Simultaneous phosphorylation and Bi modification of BiOBr for promoting photocatalytic CO₂ reduction, *ACS Sustain. Chem. Eng.* 7 (2019) 14953–14961.
- [22] K. Talukdar, B.M. Jun, Y. Yoon, Y. Kim, A. Fayyaz, C.M. Park, Novel Z-scheme Ag₃PO₄/Fe₃O₄-activated biochar photocatalyst with enhanced visible-light catalytic performance toward degradation of bisphenol A, *J. Hazard. Mater.* 398 (2020), 123025.
- [23] S.C. Huang, X. Wang, Q.Q. Zhao, J.F. Zhu, C.W. Li, Y.H. He, S. Hu, M.M. Sartin, S. Yan, B. Ren, Probing nanoscale spatial distribution of plasmonically excited hot carriers, *Nat. Commun.* 11 (2020) 4211.
- [24] K. Donabauer, K. Murugesan, U. Rozman, S. Crespi, B. Konig, Photocatalytic reductive radical-polar crossover for a base-free corey-seebach reaction, *Chemistry* 26 (2020) 12945–12950.
- [25] L. Lyu, L. Zhang, C. Hu, Galvanic-like cells produced by negative charge nonuniformity of lattice oxygen on d-TiCuAl-SiO₂ nanospheres for enhancement of Fenton-catalytic efficiency, *Environ. Sci.: Nano* 3 (2016) 1483–1492.
- [26] G. Kresse, J. Furthmüller, Efficiency of ab-initio total energy calculations for metals and semiconductors using a plane-wave basis set, *Comput. Mater. Sci.* 6 (1996) 15–50.
- [27] J.P. Perdew, K. Burke, M. Ernzerhof, Generalized gradient approximation made simple, *Phys. Rev. Lett.* 77 (1996) 3865–3868.
- [28] O. Diaz-Morales, F. Calle-Vallejo, C. de Munck, M.T.M. Koper, Electrochemical water splitting by gold: evidence for an oxide decomposition mechanism, *Chem. Sci.* 4 (2013) 2334–2343.
- [29] M. Li, S. Yu, H. Huang, X. Li, Y. Feng, C. Wang, Y. Wang, T. Ma, L. Guo, Y. Zhang, Unprecedented eighteen-faceted BiOCl with a ternary facet junction boosting cascade charge flow and photo-redox, *Angew. Chem. Int. Ed. Engl.* 58 (2019) 9517–9521.
- [30] L. Zhang, Z. Wang, C. Hu, B. Shi, Enhanced photocatalytic performance by the synergy of Bi vacancies and Bi⁰ in Bi⁰₂-δMoO₆, *Appl. Catal. B: Environ.* 257 (2019), 117785.
- [31] R.A. Geioushy, S.M. El-Sheikh, A.B. Azzam, B.A. Salah, F.M. El-Dars, One-pot fabrication of BiPO₄/Bi₂S₃ hybrid structures for visible-light driven reduction of hazardous Cr(VI), *J. Hazard. Mater.* 381 (2020), 120955.
- [32] L. Yang, Y. Hu, L. Zhang, Architecting Z-scheme Bi₂S₃@CoO with 3D chrysanthemums-like architecture for both photoelectro-oxidation and -reduction performance under visible light, *Chem. Eng. J.* 378 (2019), 122092.
- [33] J.M. Song, C.-J. Mao, H.-L. Niu, Y.-H. Shen, S.-Y. Zhang, Hierarchical structured bismuth oxychlorides: self-assembly from nanoplates to nanoflowers via a solvothermal route and their photocatalytic properties, *CrystEngComm* 12 (2010) 3875–3881.
- [34] W. Li, Y. Zou, X. Geng, F. Xiao, G. An, D. Wang, Constructing highly catalytic oxidation over BiOBr-based hierarchical microspheres: importance of redox potential of doped cations, *Mol. Catal.* 438 (2017) 19–29.
- [35] W. Liu, D. Zhong, Z. Dai, Y. Liu, J. Wang, Z. Wang, J. Pan, Synergetic utilization of photoabsorption and surface facet in crystalline/amorphous contacted BiOCl-Bi₂S₃ composite for photocatalytic degradation, *J. Alloy. Compd.* 780 (2019) 907–916.
- [36] X. Dong, B. Ren, Z. Sun, C. Li, X. Zhang, M. Kong, S. Zheng, D.D. Dionysiou, Monodispersed CuFe₂O₄ nanoparticles anchored on natural kaolinite as highly efficient peroxymonosulfate catalyst for bisphenol A degradation, *Appl. Catal. B: Environ.* 253 (2019) 206–217.
- [37] X. Shi, P. Wang, L. Wang, Y. Bai, H. Xie, Y. Zhou, J. Wang, Z. Li, L. Qu, M. Shi, L. Ye, Few layered BiOBr with expanded interlayer spacing and oxygen-vacancies for efficient decomposition of real oil field produced wastewater, *ACS Sustain. Chem. Eng.* 6 (2018) 13739–13746.
- [38] F. Lei, Y. Sun, K. Liu, S. Gao, L. Liang, B. Pan, Y. Xie, Oxygen vacancies confined in ultrathin indium oxide porous sheets for promoted visible-light water splitting, *J. Am. Chem. Soc.* 136 (2014) 6826–6829.
- [39] J. Wu, X. Li, W. Shi, P. Ling, Y. Sun, X. Jiao, S. Gao, L. Liang, J. Xu, W. Yan, C. Wang, Y. Xie, Efficient visible-light-driven CO₂ reduction mediated by defect-engineered BiOBr atomic layers, *Angew. Chem. Int. Ed. Engl.* 57 (2018) 8719–8723.
- [40] L. Pan, J.J. Zou, X. Zhang, L. Wang, Water-mediated promotion of dye sensitization of TiO₂ under visible light, *J. Am. Chem. Soc.* 133 (2011) 10000–10002.
- [41] P. Tsai, K. Ichikawa, C. Mailer, S. Pou, H.J. Halpern, B.H. Robinson, R. Nielsen, G. M. Rosen, Esters of 5-carboxyl-5-methyl-1-pyrrolin N-oxide: a family of spin traps for superoxide, *J. Org. Chem.* 68 (2003) 7811–7817.